coatings

Article

Effect of the Sputtering Deposition Conditions on the Crystallinity of High-Temperature Annealed AlN Films

Kenjiro Uesugi [1,2,*], Kanako Shojiki [3,4], Shiyu Xiao [1], Shigeyuki Kuboya [1] and Hideto Miyake [2,3]

1 Strategic Planning Office for Regional Revitalization, Mie University, 1577 Kurimamachiya-cho, Tsu 5148507, Japan; xiao@sporr.mie-u.ac.jp (S.X.); kuboya.shigeyuki@mie-u.ac.jp (S.K.)
2 Graduate School of Regional Innovation Studies, Mie University, 1577 Kurimamachiya-cho, Tsu 5148507, Japan; miyake@elec.mie-u.ac.jp
3 Graduate School of Engineering, Mie University, 1577 Kurimamachiya-cho, Tsu 5148507, Japan; k.shojiki@elec.mie-u.ac.jp
4 Graduate School of Engineering, Osaka University, 1-2 Yamadaoka, Suita 5650871, Japan
* Correspondence: k.uesugi@opri.mie-u.ac.jp; Tel.: +81-59-231-6995

Abstract: Face-to-face annealed sputter-deposited aluminum nitride (AlN) templates (FFA Sp-AlN) are a promising material for application in deep-ultraviolet light-emitting diodes (DUV-LEDs), whose performance is directly related to the crystallinity of the AlN film. However, the influence of the sputtering conditions and annealing on the crystallinity of AlN films have not yet been comprehensively studied. Accordingly, in this study, we fabricate AlN films on sapphire substrates through sputtering deposition followed by face-to-face high-temperature annealing, and investigate the influence of the sputtering conditions, such as the sputtering gas species and chamber pressure, on the crystallinity of the AlN films before and after annealing. The results revealed that reducing the amount of Ar in the sputtering gas significantly enhances the *c*-axis oriented growth during the initial stages of sputtering deposition and mitigates the tilt disorder of the layer deposited on the initial layer, resulting in low threading dislocation densities (TDDs) in the annealed AlN films. Decreasing the chamber pressure also effectively improves the crystallinity of the annealed AlN films. Thus, although high-temperature annealing can reduce the TDDs in AlN films, the properties of the as-sputtered AlN films have a significant effect on the crystallinity of FFA Sp-AlN films.

Keywords: AlN; sapphire; radio frequency sputtering; face-to-face annealing; crystallinity; X-ray diffraction; atomic force microscopy; deep-ultraviolet light-emitting diodes

check for updates

Citation: Uesugi, K.; Shojiki, K.; Xiao, S.; Kuboya, S.; Miyake, H. Effect of the Sputtering Deposition Conditions on the Crystallinity of High-Temperature Annealed AlN Films. *Coatings* **2021**, *11*, 956. https://doi.org/10.3390/coatings11080956

Academic Editor: Alessio Lamperti

Received: 16 July 2021
Accepted: 9 August 2021
Published: 10 August 2021

1. Introduction

Aluminum nitride (AlN) is considered to be an attractive material owing to its physical characteristics such as an ultrawide bandgap energy, a transparency to deep-ultraviolet (DUV) light, superior thermal conductivity, large piezoelectric response, and thermal and chemical stability. Recently, III-nitride-based DUV light-emitting diodes (LEDs) have received significant attention for sterilization and disinfection applications [1,2]. To fabricate DUV-LEDs with high efficiency and long-term reliability, the crystallinity of AlGaN, which acts as the light-emitting layer and the electrically conductive layer, must be improved [3,4]. The crystallinity of AlGaN is significantly influenced by that of the underlying AlN buffer layer. Therefore, the preparation of high-quality AlN templates can improve the performance of DUV-LEDs. Although free-standing AlN substrates fabricated through the sublimation method already possess threading dislocation densities (TDDs) of 10^3–10^5 cm^{-2} [5], these free-standing substrates cannot be realistically employed in industrial mass production as the bulk crystals are extremely expensive and are available only up to a diameter of 5.08 cm (2 inches). Therefore, AlN templates with a high crystallinity should be fabricated on foreign substrates such as sapphire. Various growth techniques for AlN films have been developed using conventional methods such as metalorganic vapor phase epitaxy

(MOVPE) or hydride vapor phase epitaxy (HVPE), but the TDDs of AlN on sapphire substrates are still approximately 10^8 cm^{-2} owing to a large lattice mismatch between AlN and sapphire [6]. Consequently, alternative schemes, such as post-deposition high-temperature annealing, have been developed to synthesize AlN films on sapphire with low TDDs. During high-temperature annealing at approximately 1700 °C, rearrangement of atoms and recrystallization occur in the AlN film [7]. Consequently, the numerous threading dislocations (TDs) that initially exist in the AlN films are diminished. Studies have shown that high-temperature annealing is not only effective for MOVPE-grown AlN but also for sputter-deposited AlN [8]. Furthermore, a face-to-face annealing setup prevents the AlN film from undergoing thermal decomposition under extremely high temperatures and enables the annealing of the AlN films at 1013 hPa in an N_2 atmosphere [8]. Face-to-face annealed sputter-deposited AlN templates (FFA Sp-AlN) are a promising low-cost and high-quality alternative AlN template for DUV-LED applications. Multiple studies have reported that DUV-LEDs using FFA Sp-AlN with low TDDs have better performance than those using conventional MOVPE-grown AlN templates with relatively high TDDs [9,10].

Several researchers, including us, have reported on the high-temperature annealing of AlN thin films on sapphire substrates. The AlN deposition methods used in these studies can vary significantly, from radio frequency (RF) sputtering [11–18], to direct current (DC) sputtering [19], MOVPE [20–23], and molecular beam epitaxy (MBE) [24]. A combination of sputtering and MOVPE has also been used, e.g., annealing of homoepitaxially MOVPE-grown AlN on a thin AlN buffer deposited by sputtering [25–27]. Nevertheless, the general consensus in all these studies is that high-temperature annealing improves the crystallinity of AlN. Furthermore, most of these studies indicate that the higher the annealing temperature and the longer the annealing time, the better the crystallinity of the AlN. However, the reported crystallinity after high-temperature annealing varies across these studies, even if the annealing conditions were similar. Therefore, the influence of the crystallinity of AlN before annealing on that of after annealing must be clarified to fabricate AlN templates with high crystallinity after high-temperature annealing.

In our previous research, we reported that the TDDs in FFA Sp-AlN can be reduced by increasing the sputtered AlN film thickness [15–17]. However, the current understanding of the relationship between the sputtering conditions and the crystallinity of FFA Sp-AlN is quite limited [18] and has not yet been discussed in detail. To the best of our knowledge, there are no comprehensive studies on the crystallinity of AlN sputtered films using RF sputtering with an AlN sintered target and on that of AlN after annealing. In this study, we fabricated AlN films through sputtering, with various supplied gas species at various chamber pressures, followed by high-temperature annealing, and compared the crystallinities of the AlN films before and after annealing. The results indicate that the deposition conditions and properties of the as-sputtered AlN films have a significant effect on the final crystallinity of FFA Sp-AlN.

2. Materials and Methods

AlN films were deposited through RF sputtering on *c*-plane sapphire substrates with a surface off-cut angle of 0.2° relative to the *m*-axis. The diameter of the substrates was 5.08 cm (2 inches). Figure 1a shows the schematic illustration of the sputtering system. Polycrystalline sintered AlN (99.9%) was used as the source target for the RF sputtering, and the distance from the target to the substrate (T–S) was 14 cm. The substrates were set in a face-down arrangement. The background pressure of the sputtering chamber was less than 6.0×10^{-5} Pa. Pure N_2 or N_2–Ar mixtures were used as the sputtering gases. N_2 was prepared by passing the vaporized liquid nitrogen through an inert gas purifier. Ar was supplied directly from the cylinder. The nominal purity of the N_2 and Ar was higher than 99.99999% (7N) and 99.9999% (6N), respectively. When using pure N_2, Ar was introduced only at the time of the ignition of RF-plasma. During AlN deposition, the substrate temperature and RF power were maintained at 600 °C and 700 W, respectively. Two groups of AlN films were fabricated herein: in the first group, 330 nm-thick AlN films were deposited under a fixed sputtering pressure of 0.1 Pa, using various $N_2/(N_2 + Ar)$ ratios ranging from 25% to 100%; in the second group, 185–245 nm-thick AlN films were deposited under various sputtering pressures ranging from 0.05 to 1.5 Pa. For the second group, only N_2 was used as the sputtering gas. The gas flow supplied during the fabrication of the samples was maintained at 24 sccm. The sputtering pressure was controlled by a tunable conductance bulb placed between the sputtering chamber and the vacuum pump. After deposition, high-temperature face-to-face annealing was performed at 1700 °C in an N_2 atmosphere at 1013 hPa for 3 h. Figure 1b shows the schematic illustration of the experimental setup for face-to-face annealing. Subsequently, X-ray diffraction (XRD) was performed using an X'pert MRD (Malvern Panalytical, Malvern, UK) with an X-ray mirror and channel-cut Ge(220) 2-bounce monochromator to characterize the crystallinity and lattice constants of the AlN films. Herein, $CuK_{\alpha1}$ radiation (λ = 0.15406 nm) was used as the X-ray source. A channel-cut Ge(220) 3-bounce analyzer and Xe proportional detector were used to measure the high-resolution X-ray rocking curve (XRC), and a one-dimensional semiconductor array detector was used to measure the XRD reciprocal space map (XRD-RSM). The ideal smallest XRC full width at half maximum (FWHM) value of the AlN(0002) diffraction with the experimental setup used herein was approximately 9 arcsec. During the XRD measurement, the X-ray irradiation area on the AlN film was smaller than 1.1 mm (the length parallel to the X-ray irradiation direction) × 1.6 mm (the width perpendicular to the X-ray irradiation direction) for the high-resolution XRC setup and smaller than 0.4 mm × 6.5 mm for the XRD-RSM setup. An MFP-3D atomic force microscope (AFM) (Oxford instruments, Abington, UK) was used to investigate the surface morphology of the samples. The AFM measurements were carried out in the AC mode. The XRD and AFM characterizations were performed on the center of each sample. However, the crystallinity and surface morphology of the samples were uniform except for the area 5 mm from the periphery of the wafers. Additionally, regardless of the sputtering conditions, it was confirmed by optical microscope observation that there was no crack or volcano-shaped macroscopic defect [14,17] on the AlN, neither before nor after annealing.

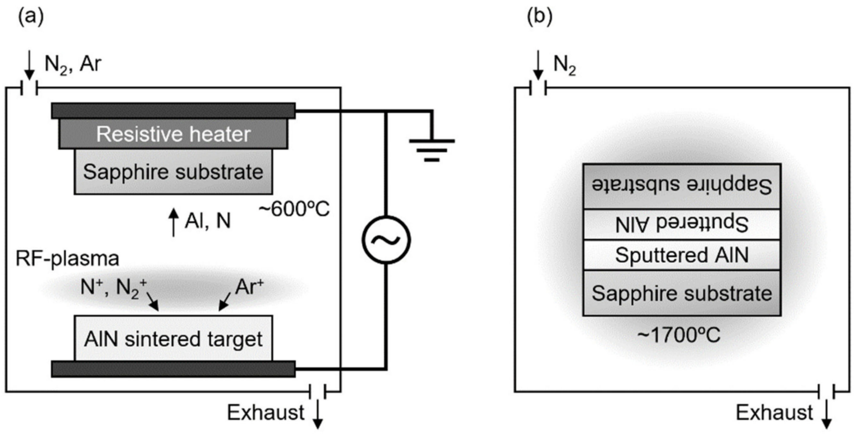

Figure 1. Schematic illustrations of (**a**) RF sputtering system for AlN deposition, and (**b**) face-to-face annealing.

3. Results and Discussion

3.1. Effect of Sputtering Gas Species

In this section, we discuss the relationship between the supplied N_2–Ar ratio and the characteristics of the AlN films before and after annealing. The deposition rate of the AlN varied with the N_2–Ar ratio. As the $N_2/(N_2 + Ar)$ ratio increased from 25% to 100%, the deposition rate decreased from 4.0 to 2.7 nm/min. The N_2–Ar ratio influences the deposition rate owing to the difference in the sputtering effectiveness of the N atom and the Ar atom. However, as an AlN sintered target was used herein, the change in the deposition rate with the variation in the $N_2/(N_2 + Ar)$ ratio was not as significant as that usually observed during reactive sputtering with an Al metal target. The deposition duration was modified based on the $N_2/(N_2 + Ar)$ ratio to achieve a uniform AlN film thickness.

Prior to performing FFA, we investigated the crystallinity of the as-sputtered AlN films. The as-sputtered AlN and FFA Sp-AlN in this study exhibited a wurtzite (hexagonal) rather than a zincblende (cubic) structure. Its phase was confirmed by the existence of XRD peaks from specific asymmetric diffractions. Figure 2 shows the XRD-RSM images of the as-sputtered AlN films that were sputtered using $N_2/(N_2 + Ar)$ ratios of 25% and 100%. The AlN(0002), AlN(0004), and AlN(0006) symmetric diffractions were characterized herein. As shown in the RSM images of the (0002) diffraction, the diffraction peak comprised two characteristic peaks. One was a streaked signal extending from the top of the peak at $q_c \approx 0.402$ to the origin of the reciprocal space, and the other peak broadened toward the q_a direction. The streaked signal diffracted from the highly c-axis oriented thin quasi-coherent AlN layer just above the sapphire substrates [28,29]. The quasi-coherent layer inherited the flatness and excellent crystallinity of the sapphire substrate. Compared to those of the unstrained bulk AlN (c = 4.9808 Å, q_c = 0.40154 [5]), the streaked characteristic and smaller q_c value of the quasi-coherent layer in the RSM image reflect its compressive stress and graded c-axis lattice constant. In contrast, the broad peak in the RSM image is related to the relaxed layer that exists above the quasi-coherent layer. This relaxed layer has a smaller c-axis lattice constant (larger q_c value) than the bulk AlN. The broad feature toward the q_a direction reflects its out-of-plane orientational disorder (crystalline tilt) or a small in-plate correlation length. Comparing the two RSM images, the AlN sputtered using pure N_2 had a stronger signal intensity from the quasi-coherent layer compared to the sample that was sputtered using the N_2–Ar gas mixture. The difference between the two samples was more pronounced in the RSM images of the higher-order diffractions. For example, in the (0004) and (0006) diffractions of the $N_2/(N_2 + Ar)$ = 25% samples (Figure 2b,c), only the signal from the relaxed layer can be observed. However, in the (0004) and (0006) diffractions of the $N_2/(N_2 + Ar)$ = 100% samples (Figure 2e,f), the streak feature of the quasi-coherent layer could be identified as well. This is possibly because the quasi-coherent layer of the sample sputtered using pure N_2 had a larger thickness or higher crystallinity than the sample sputtered using the N_2–Ar mixture.

High-resolution XRC measurements were performed to quantitatively evaluate the effect of the sputtering gas on the as-sputtered AlN films. Figure 3a shows the XRC profiles of the AlN(0002) diffraction obtained using an analyzer crystal placed in front of the detector. The XRC profiles correspond to the cross-sectional profiles of the RSM images formed horizontally along the q_a axis at q_c = 0.40170 and q_c = 0.40198, which passed through the intensity peaks of the RSM images. The AlN(0002) XRC profiles represent the tilt component of the crystalline orientation disorder. The sharp specular peak that originated from the quasi-coherent layer and the broad wing peak with relatively low intensity that originated from the relaxed layer can be observed in the XRC profiles. Similar profiles have been reported for an ErAs/GaAs system [30], MOVPE-grown AlN on sapphire [31], and sputter-deposited AlN on sapphire [13,32]. As shown in the RSM images, the intensity of the sharp peak was higher for the film that was deposited using pure N_2 than for that using the N_2–Ar mixture. Furthermore, the line width of the broad peak for the N_2-sputtered sample was narrower than that for the N_2–Ar-sputtered sample. The XRC profiles were fitted as a superposition of a sharp peak (Gaussian) and a broad peak (Lorentzian or pseudo-Voigt function). The peak intensities and the FWHM of each peak were derived to evaluate the crystallinity of the quasi-coherent and relaxed layers. Figure 3b shows the peak intensity of the sharp peak and FWHM values of both the sharp peak and the broad peak as a function of the $N_2/(N_2 + Ar)$ ratio. The intensity of the sharp peak increased monotonically as the $N_2/(N_2 + Ar)$ ratio increased. In contrast, the FWHM values of the sharp peaks were between 9.5 and 11.4 arcsec for all the samples. As the values are approximately the same for the resolution limit of the XRD system, it can be concluded that there is no clear dependence on the $N_2/(N_2 + Ar)$ ratio. Thus, the tilt disorder of the quasi-coherent layer is small regardless of the $N_2/(N_2 + Ar)$ ratio; however, compared to the samples sputtered using pure N_2, the quasi-coherent layer in the samples sputtered using the N_2–Ar mixture easily transitioned to the relaxed layer with a lesser thickness.

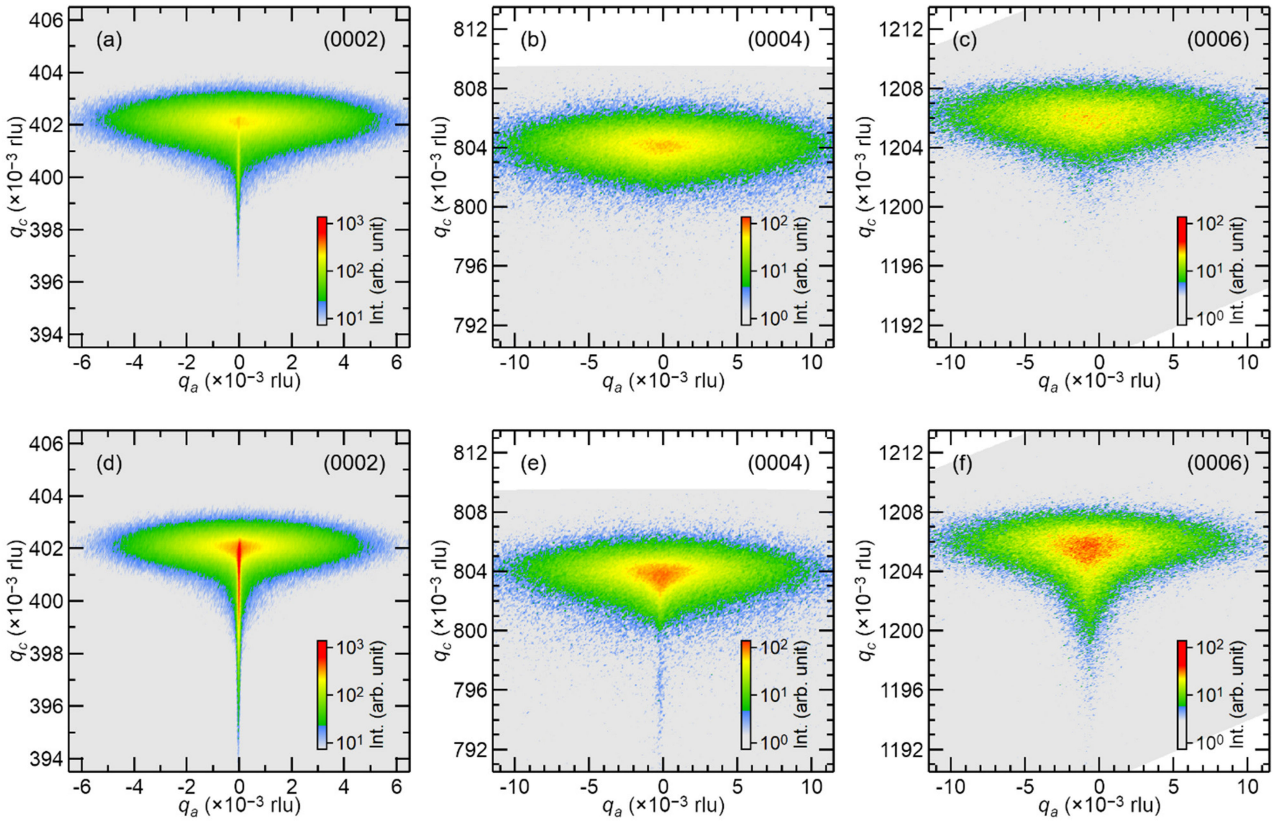

Figure 2. X-ray diffraction reciprocal space map (XRD-RSM) images of (**a**,**d**) AlN(0002); (**b**,**e**) AlN(0004); and (**c**,**f**) AlN(0006) diffractions of as-sputtered AlN films using $N_2/(N_2 + Ar)$: (**a**–**c**) 25% and (**d**–**f**) 100%.

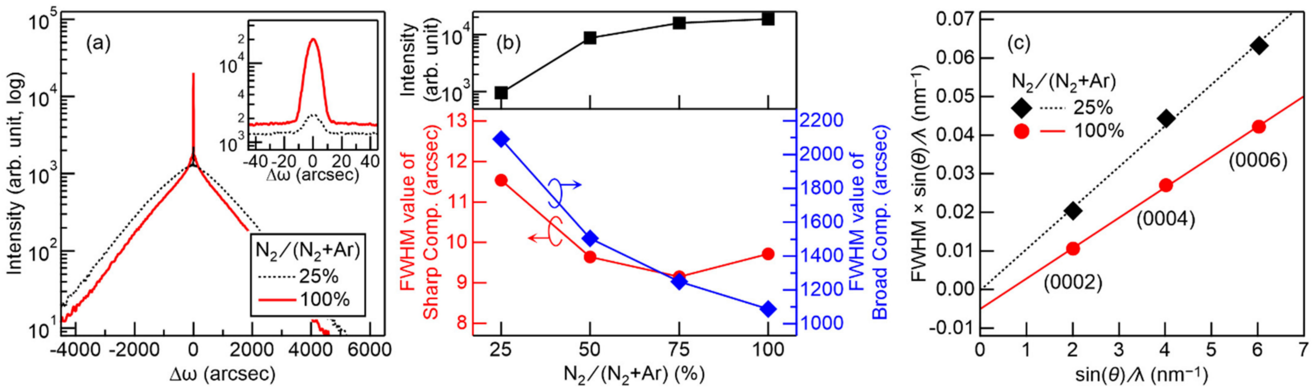

Figure 3. (**a**) High-resolution X-ray rocking curve (XRC) profiles of AlN(0002) diffraction of the as-sputtered AlN films using $N_2/(N_2 + Ar)$ ratios of 25% and 100% that were measured at a fixed value of 2θ to include the peak top of the RSM images shown in Figure 2. The inset shows the enlarged profiles of the sharp component. (**b**) Effect of $N_2/(N_2 + Ar)$ ratio on the peak intensity of the sharp component and XRC full width at half maximum (XRC-FWHM) values of the sharp component and broad component of the AlN(0002) diffraction. (**c**) Williamson–Hall plot of as-sputtered AlN films: for (0002) diffraction, the FWHM values of the broad component in the high-resolution XRC profiles shown in (**a**) were used; for the (0004) and (0006) diffractions, the FWHM values were evaluated from the XRD-RSM images shown in Figure 2. The lines are the linear fit.

Unlike those of the quasi-coherent layer, the FWHM values of the relaxed layer decreased with the increase in the $N_2/(N_2 + Ar)$ ratio. The higher-order diffractions were investigated to reveal the origin of the broadening of the broad peak. Unfortunately, the intensities of the diffracted X-rays from the AlN(0004) and (0006) diffraction planes were too weak to characterize using the high-resolution setup. Consequently, the XRC-FWHM values of these diffractions were evaluated from the transverse cross-sectional profiles of the XRD-RSM images shown in Figure 2b,c,e,f. The XRC profiles of the higher-order diffractions (not shown here) did not present sharp specular peaks, which is in accordance with existing research. Figure 3c depicts the Williamson–Hall plots [33] of two AlN films that were sputtered using $N_2/(N_2 + Ar)$ ratios of 25% and 100%. The FWHM of the AlN(0002) diffraction represents the value of the broad peak. The slope of the fitted line reflects the tilt disorder. On the contrary, the intercept of the fitted line corresponds to the inverse of the in-plane correlation length [34,35]. One sample exhibited almost no intercepts, whereas the other exhibited invalid negative intercepts. Therefore, the FWHM of the broad peak from the (0002) diffraction was possibly underestimated. Nevertheless, the influence of the in-plane correlation length can be ignored, and the tilt disorder of the relaxed layer is the dominant factor that influences the FWHM values of the broad peaks. Furthermore, the magnitude of the slope of the linear fitting and the absolute value of the XRC-FWHM were consistent. Consequently, the tilt disorder of the relaxed layer can be evaluated from the XRC-FWHM values of the broad peaks.

Based on the results shown in Figures 2 and 3, it can be inferred that the presence of Ar atoms in the sputtering gas reduces the thickness of the quasi-coherent layer. Furthermore, the reduced thickness of the quasi-coherent layer and (or) the presence of Ar in the sputtering gas enhances the crystalline tilt disorder of the relaxed layer. Notably, the XRC-FWHM values of the AlN($10\bar{1}2$) diffractions (not shown here), which include the in-plane orientational disorder, i.e., crystalline twist, are independent of the $N_2/(N_2 + Ar)$ ratio. Regardless of the $N_2/(N_2 + Ar)$ ratio, all the samples had FWHM values of approximately 6000 arcsec.

The crystallinity of the samples was analyzed again after performing FFA. Figure 4a shows the XRC profiles of the (0002) diffraction of the FFA Sp-AlN. Similar to the as-sputtered AlN films, each FFA Sp-AlN sample had two components in the XRC profiles. However, comparing the as-sputtered AlN and FFA Sp-AlN films, the intensity of the broad peak relative to that of the sharp peak was lower, and the width of the broad peak was narrower as well. These changes in the XRC profiles can be attributed to the improvement in the crystallinity of the AlN films after FFA. Similar to the analysis performed on the as-sputtered samples, the XRC profiles of the FFA Sp-AlN samples were fitted as a superposition of two Gaussian peaks. Figure 4b shows the peak intensity of the sharp peak and the FWHM values of both the sharp peak and the broad peak as a function of the $N_2/(N_2 + Ar)$ ratio. The trends of the FFA Sp-AlN samples are similar to those of the as-sputtered samples (shown in Figure 3b): the intensity of the sharp peak is higher, and the peak width of the broad peak becomes narrower as the $N_2/(N_2 + Ar)$ ratio increases. Figure 4c shows the Williamson–Hall plot of the broad peaks of the two FFA Sp-AlN films corresponding to the samples shown in Figure 3c. In the FFA Sp-AlN samples, the diffracted X-ray intensity increased to the extent that high-resolution XRC characterization could be performed even on the higher-order diffractions. Consequently, the FWHM values of all the diffractions were evaluated from the XRC profiles. The FFA Sp-AlN samples that were sputtered using pure N_2 exhibited sharp peaks on the (0004) and (0006) diffractions, whereas those that were sputtered using N_2–Ar did not exhibit sharp peaks. Consequently, these profiles were fitted using a single pseudo-Voigt function as the entire profile was in the form of a broad peak. The FFA Sp-AlN samples that were sputtered using an $N_2/(N_2 + Ar)$ ratio of 25% exhibited a relatively small intercept compared to the slope of the linear fit. The dominant factor of the broadening of the broad peak was the tilt disorder, which is similar to the as-sputtered samples. The FFA Sp-AlN samples that were sputtered using an $N_2/(N_2 + Ar)$ ratio of 100% exhibited a small slope that corresponds to approximately 10 arcsec of tilt disorder. Therefore, the FWHM values of the broad peaks of the FFA Sp-AlN samples that were sputtered using a high $N_2/(N_2 + Ar)$ ratio do not accurately reflect the tilt disorder but influence the broadening of the peak owing to the in-plane correlation length. The

Williamson–Hall plot contained some error as the samples herein exhibited a complex structure, with multiple layers of different crystallinities stacked in the growth direction. Therefore, there are some points which cannot be explained concisely. For example, the as-sputtered AlN film exhibited invalid negative intercepts. In addition, the FFA Sp-AlN films sputtered using pure N_2 exhibited a smaller in-plane correlation length than those sputtered using N_2–Ar mixture, even though the crystallinity of the FFA Sp-AlN films sputtered using pure N_2 is higher. Nevertheless, the AlN films sputtered using Ar exhibited a larger tilt disorder than those sputtered using pure N_2. Furthermore, the tilt remained even after FFA. Figure 4d shows the effect of the $N_2/(N_2 + Ar)$ ratio on the (10−12) XRC-FWHM values of the FFA Sp-AlN. Compared to the (10−12) FWHM values of the as-sputtered samples, those of the FFA Sp-AlN exhibited a clear dependence on the $N_2/(N_2 + Ar)$ ratio. Furthermore, the reduction in the FWHM values with the increase in the $N_2/(N_2 + Ar)$ ratio was confirmed.

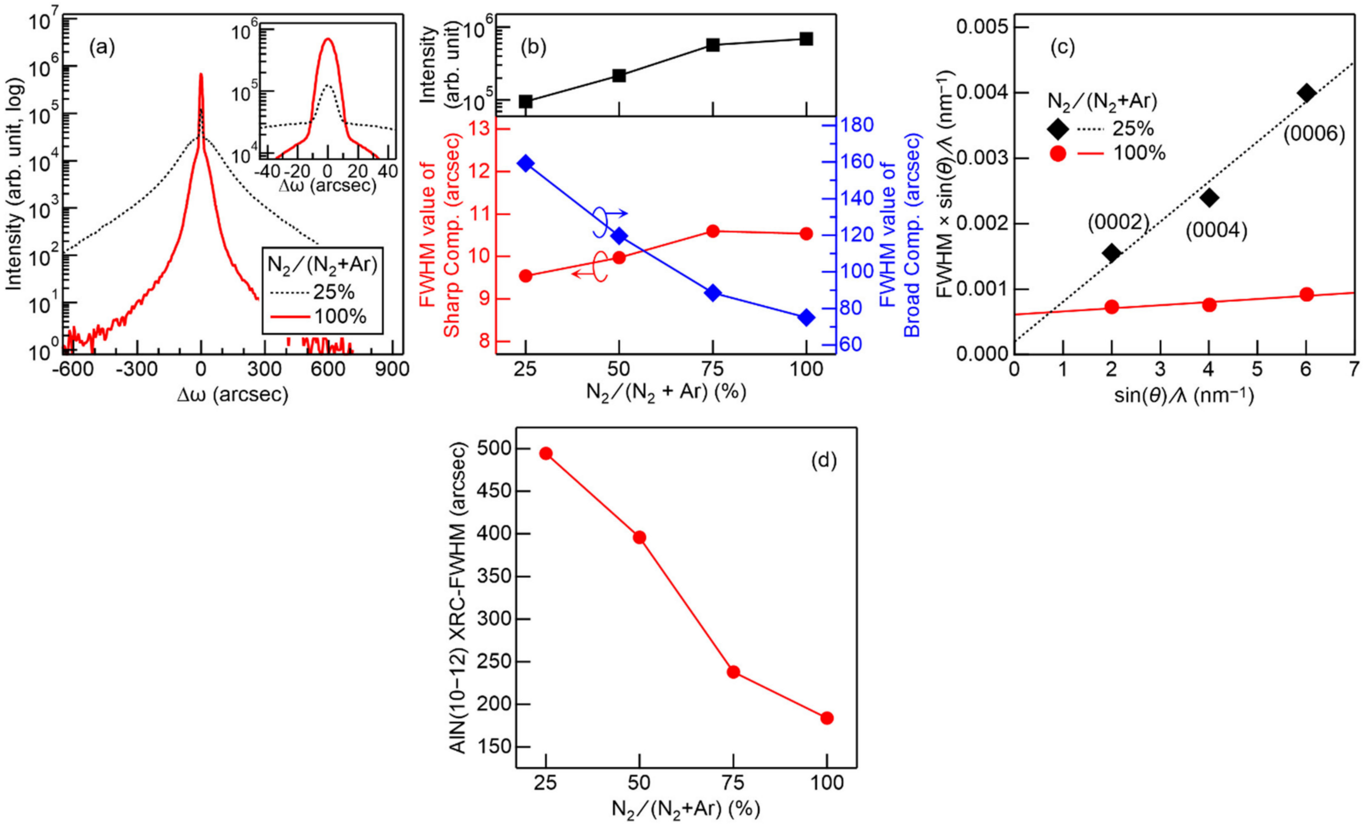

Figure 4. (**a**) High-resolution XRC profiles of AlN(0002) diffraction of the face-to-face annealed sputter-deposited AlN template (FFA Sp-AlN) that was deposited using $N_2/(N_2 + Ar)$ = 25% and 100%. The inset shows the enlarged profiles of the sharp component. (**b**) Effect of $N_2/(N_2 + Ar)$ ratio on the peak intensity of the sharp component and XRC-FWHM values of the sharp component and broad component of the AlN(0002) diffraction. (**c**) Williamson–Hall plot of the FFA Sp-AlN samples. The FWHM values of the broad component in the high-resolution XRC profiles were used for all the diffractions, as long as the sharp component was visible. If the XRC profiles only contain one component, the FWHM value is that of the entire profile. The lines are the linear fit. (**d**) Relationship between AlN(10−12) XRC-FWHM values of FFA Sp-AlN and the $N_2/(N_2 + Ar)$ ratio of the sputtering gas.

Figure 5 shows the AFM images of the FFA Sp-AlN samples that were sputtered using various $N_2/(N_2 + Ar)$ ratios. All the samples exhibited step-and-terrace structures and had similar surface root mean square (RMS) roughness values of less than 0.25 nm. However, the shape of the step-and-terrace structures changed with the $N_2/(N_2 + Ar)$ ratio; the step-and-terrace structures of the samples deposited using pure N_2 was straight and continuous from the top to the bottom of the AFM image, whereas those of the samples deposited using Ar were winding and interrupted in some places. In Figure 5e, which is an enlarged image of a portion of Figure 5a, the step interruptions are indicated by white arrows. The step interruptions reflect the existence of TDs, wherein the Burgers vector includes c components, such as screw-type (type-c) and mixed-type (type-$a + c$) dislocations on the film surface. The dominant TDs in the FFA Sp-AlN samples were edge-type dislocations. However, the screw- and mixed-type dislocations deteriorate the surface flatness of $Al_xGa_{1-x}N$ grown on FFA Sp-AlN as they become the origin of spiral-growth-induced hillock structures [36]. The degraded surface flatness has several adverse effects on the performance of light-emitting devices, such as a decline in the internal quantum efficiency and spectral line broadening [37].

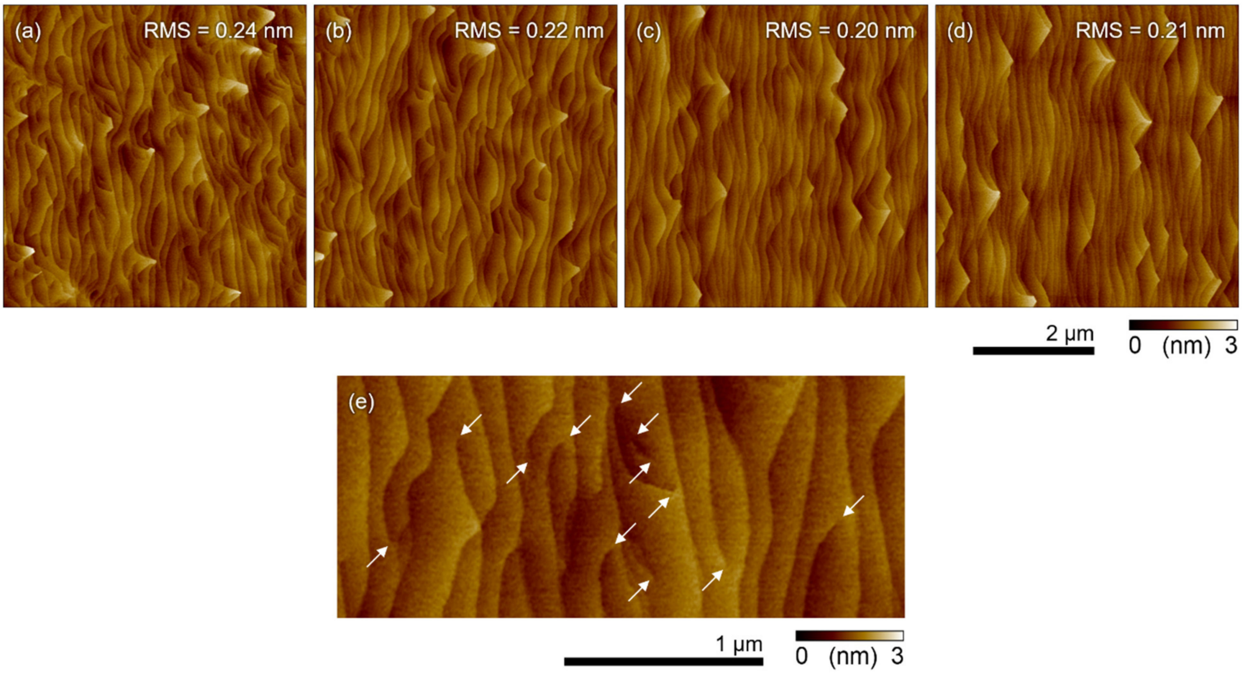

Figure 5. Atomic force microscopic (AFM) images of FFA Sp-AlN samples deposited using $N_2/(N_2 + Ar)$ ratios of: (**a**) 25%, (**b**) 50%, (**c**) 75%, and (**d**) 100%. The scale bar and height scale for (**a**–**d**) are uniform. (**e**) Magnified image of (**a**). The white arrows indicate step terminations that correspond to screw- or mixed-type dislocations.

If the FWHM values of the sharp peaks in the XRC profiles of the symmetric diffractions correctly reflect the crystalline tilt disorder of AlN, then the four samples should have a similar tilt. However, as shown in the AFM images in Figure 5, the screw- and mixed-type dislocation densities of the samples are clearly different, in that these densities decrease with an increase in the $N_2/(N_2 + Ar)$ ratio. This trend is similar to that of the FWHM values of the broad peaks shown in Figure 4b. Consequently, the FWHM values of the broad peaks plausibly reflect the tilt disorder of the AlN samples. Using Ar as the sputtering gas can improve the deposition rate, which can improve throughput and reduce the production costs. However, the degradation of the crystallinity outweighs these benefits. Therefore, to achieve the best possible crystallinity in FFA Sp-AlN, pure N_2 should be used as the sputtering gas.

3.2. *Effect of Sputtering Chamber Pressure*

This section discusses the effect of the sputtering pressure on the crystallinity of AlN films. In our previous research, we varied the sputtering pressure from 0.03 to 0.4 Pa, and reported that controlling the stress accumulated in AlN thin films by reducing the sputtering pressure can suppress crack generation during FFA [15]. Considering the crystallinity of AlN after high-temperature annealing, the XRC-FWHM values of the AlN(0002) (only the sharp component) and (10−12) diffractions did not show any significant dependence on the sputtering pressure. Compared to the sputtering pressure, the thickness of the AlN films had a stronger effect on the crystallinity of FFA Sp-AlN. In this study, the sputtering pressure was increased up to 1.5 Pa, and the XRC profiles of the AlN films before and after FFA were analyzed in detail to comprehensively investigate the effect of the sputtering pressure on the crystallinity of AlN films.

Before discussing the crystallinity, we analyzed the relationship between the strain in the as-sputtered AlN films and the sputtering pressure. Figure 6a illustrates the effect of the sputtering pressure on the lattice constants *a* and *c* of the as-sputtered AlN. The thicknesses of the AlN films are also shown in Figure 6a because it is known that they also affect the strain in as-sputtered AlN [15]. The in-plane and out-of-plane lattice constants were characterized through XRD-RSM of the AlN(10−15) asymmetric diffraction. The lattice constants here are those of the relaxed layer as the diffraction from the quasi-coherent layer does not appear clearly in the asymmetric diffraction before FFA. The lattice constant *a* increased with the increase in sputtering pressure and was maximum at 0.4 Pa. The lattice constant *c* exhibited the exact opposite behavior to that of *a*. At sputtering pressures of 0.05–1.5 Pa, *a* was larger, and *c* was smaller than that of unstrained bulk AlN. Therefore, the AlN was subjected to tensile stress, which was maximum at 0.4 Pa. In our previous work, the FFA Sp-AlN sputtered at 0.2 (with 236 nm thickness) and 0.4 Pa (223 nm thickness) exhibited a few cracks [15]. However, in this work, the FFA Sp-AlN sputtered at 0.2 (238 nm thickness) and 0.4 Pa (186 nm thickness) did not exhibit any crack. On the 0.2 Pa samples, the threshold thickness on the occurrence of the crack may be quite close to the thicknesses of these two samples, and might be affected by the slight fluctuations of the sputtering conditions. On the 0.4 Pa samples, the reduction of the film thickness contributed to the suppression of the cracking. When the sputtering pressure was 0.4 Pa or higher, the lattice constant *a* decreased with the increase in sputtering pressure, which is the opposite tendency to that observed in the previous work [15]. The strain dependence on the AlN thickness, which was observed in the previous work [15], also cannot explain the tendency. Therefore, we suspect that some changes in the crystallinity of the as-sputtered AlN films, such as an enlargement of the tilt disorder or an increase in the impurity concentrations, might contribute to the relief of the tensile stress in the as-sputtered AlN films.

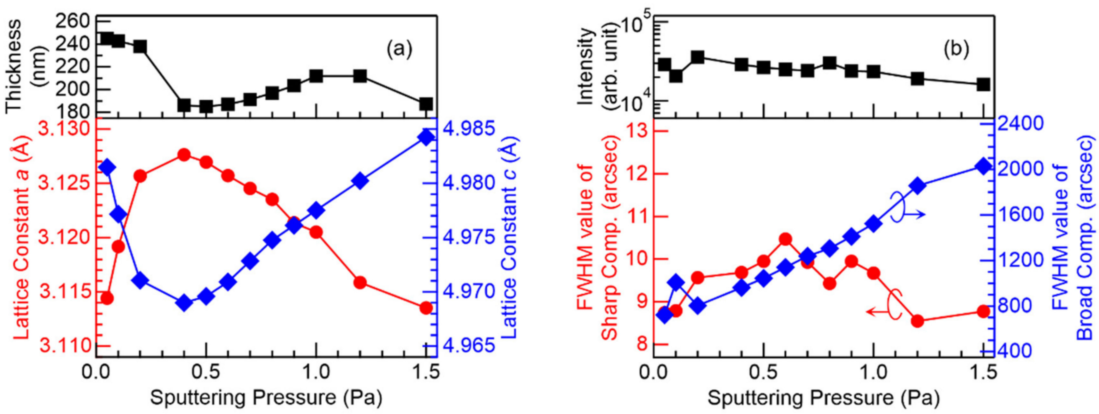

Figure 6. (**a**) Thicknesses of AlN films sputtered at various sputtering pressures, and effect of sputtering pressure on lattice constants *a* and *c* of the as-sputtered AlN film. (**b**) Effect of sputtering pressure on the peak intensity of the sharp component, and XRC-FWHM values of the sharp and broad components in the AlN(0002) diffraction.

Considering that the samples were sputtered at various sputtering pressures, the XRC profiles of the AlN(0002) diffraction before FFA had a similar shape to that of the profiles shown in Figure 3a, comprising two components that correspond to the quasi-coherent layer and the relaxed layer. Figure 6b depicts the intensity of the sharp peaks and the FWHM values of each peak as a function of the sputtering pressure. Similar to the N_2–Ar dependence curve shown in Figure 3b, the FWHM values of the quasi-coherent layer were independent of the sputtering pressure. The peak intensity of the quasi-coherent layer slightly decreased and the FWHM value of the relaxed layer increased as the sputtering pressure increased, which is qualitatively the same behavior as that due to the increase in Ar supply. Considering the XRC-FWHM values of the AlN(10−12) diffraction, the samples sputtered at 0.05 and 0.1 Pa had relatively small values (4800 and 5600 arcsec, respectively), whereas the other samples had almost the same FWHM values of 6000–6500 arcsec, regardless of the sputtering pressure.

Figure 7a presents the XRC profiles of the (0002) diffraction of FFA Sp-AlN sputtered at various sputtering pressures. The AlN deposited at a relatively low sputtering pressure of less than 0.5 Pa consisted of two components, which is similar to the XRC profiles shown in Figure 4a. However, above a sputtering pressure of 0.5 Pa, the line width and relative intensity of the broad peak increased with the increase in sputtering pressure. Finally, when the sputtering pressure exceeded 1.0 Pa, no sharp peaks were visible. Figure 7b,c demonstrate the dependence of the FWHM values of the (0002) and (10−12) diffractions, respectively, on the deposition pressure. The FWHM values of both diffractions increased with the increase in sputtering pressure, especially in the samples that were deposited at above 0.5 Pa. Furthermore, the peak intensity of the sharp peak decreased drastically. The same trend of a decrease in crystallinity with the increase in sputtering pressure was reported in [18].

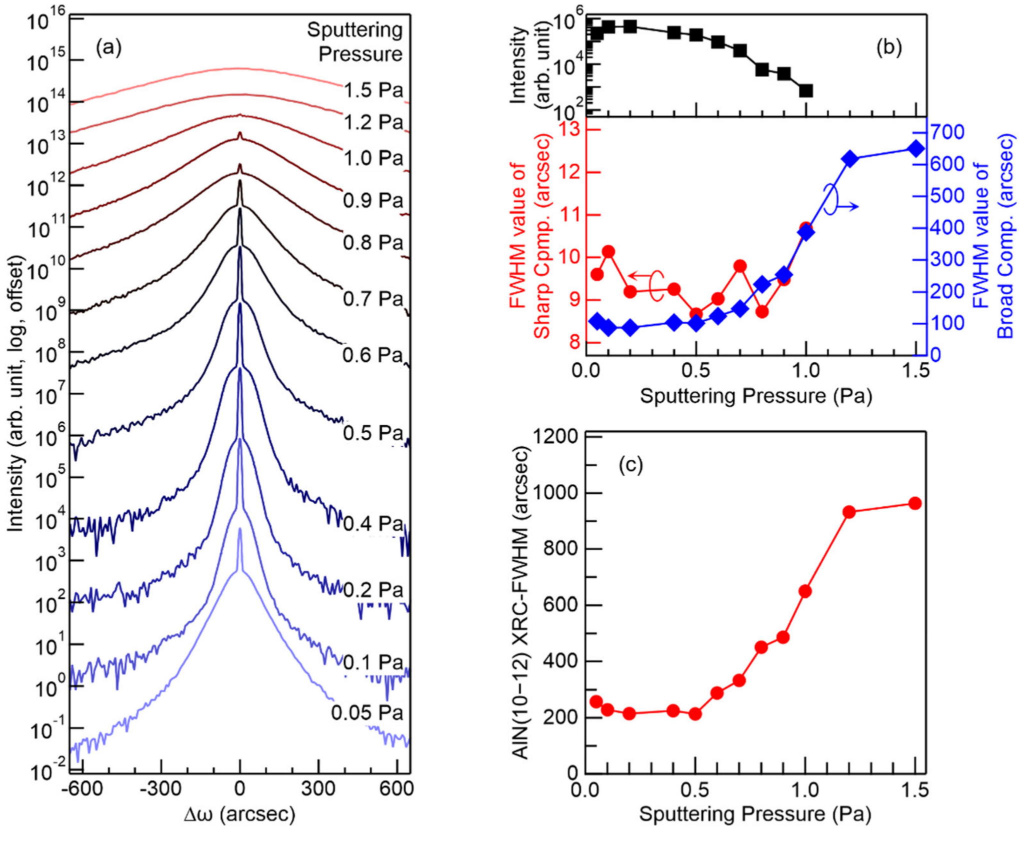

Figure 7. (**a**) Sputtering pressure dependent high-resolution XRC profiles of FFA Sp-AlN considering the AlN(0002) diffraction. (**b**) Effect of sputtering pressure on the peak intensity of the sharp component and XRC-FWHM values of the sharp component and broad component of the AlN(0002) diffraction. (**c**) Relationship between AlN(10−12) XRC-FWHM values of FFA Sp-AlN and sputtering pressure.

Figure 8 shows the AFM images of the FFA Sp-AlN that was deposited at the sputtering pressures of 0.2–0.8 Pa. Unlike the sample deposited at 0.1 Pa (Figure 5), all the samples shown in Figure 8 had small protruding structures. These structures represent the AlONs that are formed when the oxygen in AlN reacts with AlN and precipitates on the surface of the film during annealing [38]. As the density and height of the AlON islands increase with the increase in the deposition pressure, it can be inferred that the sputtering pressure affects the concentration of the oxygen impurities in AlN. In addition, the step-and-terrace structures on the FFA Sp-AlN become irregularly shaped as the deposition pressure increases and the surface flatness decreases.

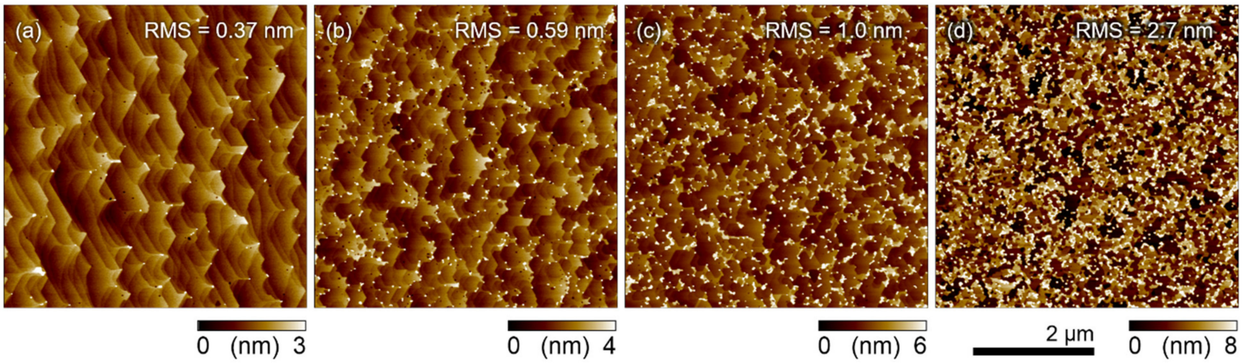

Figure 8. AFM images of the FFA Sp-AlN templates deposited at sputtering pressures of: (**a**) 0.2 Pa, (**b**) 0.4 Pa, (**c**) 0.6 Pa, and (**d**) 0.8 Pa. The scale bar is the same in all the images.

3.3. Model of Crystallinity Improvement

Based on the experimental results obtained herein, the relationship between the sputtering conditions and the crystallinity of the as-sputtered AlN and FFA Sp-AlN can be summarized as follows. The N_2–Ar ratio of the sputtering gas and the sputtering pressure affect the thickness of the quasi-coherent layer and the tilt disorder of the relaxed layer of the as-sputtered AlN. However, the twist in the as-sputtered AlN is not significantly affected by the sputtering conditions, and the twist disorder is large regardless of the sputtering conditions. Considering FFA Sp-AlN, except for the samples with poor crystallinity that are sputtered at high pressures, the AlN(0002) XRC profiles are composed of sharp peaks and broad peaks. Therefore, FFA Sp-AlN contains two kinds of regions. One originates from the quasi-coherent layer with a small tilt disorder (highly aligned region), and the other arises from the relaxed layer with a relatively large tilt disorder (tilted region). The volume of the highly aligned region and the disorder of the tilted region depend on the initial thickness of the quasi-coherent layer and the tilt disorder of the relaxed layer of the as-sputtered AlN. Furthermore, when the AlN film is sputtered at a relatively high pressure, impurities such as oxygen may be abundant, resulting in poor crystallinity of FFA Sp-AlN. Compared to FFA Sp-AlN sputtered using a low $N_2/(N_2 + Ar)$ ratio, FFA Sp-AlN sputtered at a high pressure exhibits a compatible initial tilt disorder in the relaxed layer. Additionally, the quasi-coherent layer of the FFA Sp-AlN sputtered at high pressure is thicker than that sputtered using a low $N_2/(N_2 + Ar)$ ratio. Considering these two characteristics, i.e., the thick quasi-coherent layer and the small tilt disorder in the relaxed layer before annealing, the FFA Sp-AlN sputtered at high pressure using pure N_2 should exhibit small a tilt disorder at a certain volume of the highly aligned region. However, as shown in Figure 7a, the FFA Sp-AlN sputtered at high pressure exhibited quite a large tilt disorder. Therefore, the incorporation of oxygen impurities may hinder the recovery of crystallinity. Before annealing, AlN exhibits a much larger twist disorder than a tilt disorder, and edge-type dislocations are still dominant in FFA Sp-AlN. However, the tilt disorder and the concentration of impurities in the as-sputtered AlN determine the crystallinity of FFA Sp-AlN.

Figure 9 shows a schematic diagram for improving the crystallinity of the sputter-deposited AlN films during FFA. During annealing, the highly aligned region that stems from the quasi-coherent layer should expand from the substrate side of the AlN film to the surface side. Therefore, the bottom surface of the relaxed layer is gradually incorporated into the highly aligned region by the recrystallization, using the quasi-coherent layer as the nucleation layer, and inherits its ideally small tilt disorder. In contrast, in the relaxed layer, the twist and tilt of the columnar structures in the as-sputtered AlN decrease with the pair annihilation of TDs and the expansion of the domain boundaries. However, if the initial thickness of the quasi-coherent layer is thin and the initial tilt disorder of the relaxed layer is large, the highly aligned region cannot expand sufficiently. Consequently, the relaxed layer with its relatively large tilt disorder remains tilted after FFA. Moreover, the tilted region is retained in the FFA Sp-AlN deposited at low sputtering pressure using pure N_2. Therefore, a higher annealing temperature or longer annealing time may be required to completely eliminate the tilted region [17,23]. Nevertheless, the screw- and mixed-type dislocation densities of the FFA Sp-AlN sputter-deposited at low sputtering pressure using pure N_2 are approximately two orders of magnitude lower than those of conventional MOVPE-grown AlN. Additionally, impurities may also prevent the recrystallization of the relaxed layer even though the quasi-coherent layer is sufficiently thick, and the tilt disorder of the relaxed layer is insignificant.

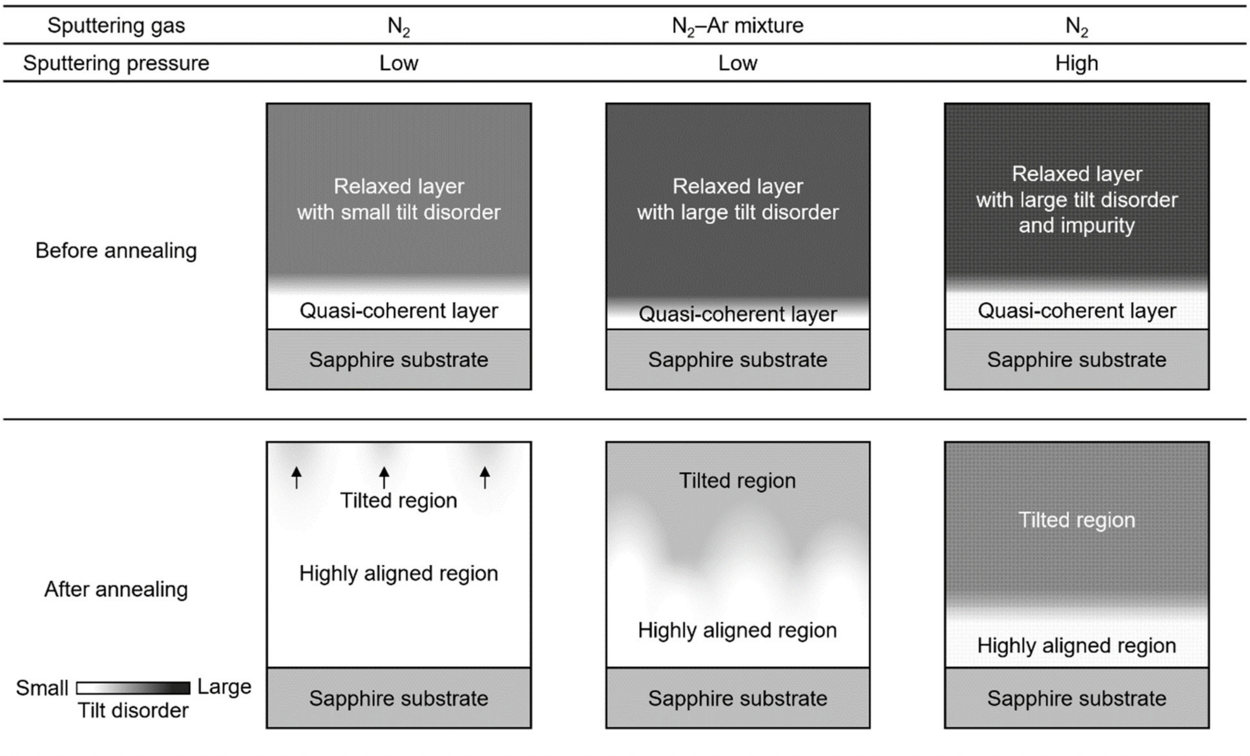

Figure 9. Schematic diagram of the tilt disorder distribution in AlN films, before and after annealing, sputtered under three typical conditions.

Thus, to achieve a sufficient recovery of crystallinity through high-temperature annealing, the tilt disorder and concentration of impurities must be considered. Moreover, the crystallinity recovery of sputter-deposited AlN on a sapphire substrate does not occur through an isotropic recrystallization process, which is observed in bulk crystals. Rather, it is affected by the quasi-coherent layer, which inherits crystalline information from the sapphire substrate.

In this work, we investigated the influence of the N_2–Ar ratio and sputtering pressure on the crystallinity of the as-sputtered and annealed AlN films. Sputtering parameters such as substrate temperature, RF power, and T–S distance, should be considered next. The FFA Sp-AlN films possess numerous impurities such as oxygen (>10^{20} cm^{-3}), carbon (>10^{19} cm^{-3}), and silicon (>10^{18} cm^{-3}) [38]. Thus, there is a possibility that the sputtering pressure not only affected the oxygen concentration but also the concentrations of other impurities and the recrystallization process. Therefore, the influence of impurity concentration should be investigated using secondary ion mass spectrometry (SIMS). Additionally, observing the recrystallization process using transmission electron microscopy (TEM) is necessary to prove the schematic model shown in Figure 9. To further improve the crystallinity of FFA Sp-AlN, a more detailed understanding of the relationship between sputtering deposition conditions, crystalline characteristics of both as-sputtered AlN and FFA Sp-AlN, and the recrystallization mechanism of the AlN film through FFA is required.

4. Conclusions

AlN films were deposited on sapphire substrates through RF sputtering using an AlN sintered target. The supply ratio of N_2 and Ar and the chamber pressure were varied during the sputtering process. The crystallinity of the as-sputtered AlN films was affected by the sputtering conditions. When pure N_2 and a lower sputtering pressure were used, a relatively thick quasi-coherent layer was formed that inherited the flatness and excellent crystallinity of the sapphire substrate. Consequently, the tilt disorder of the relaxed layer deposited over the quasi-coherent layer was mitigated. The crystallinity of the FFA Sp-AlN film is significantly affected by that of the as-sputtered AlN film. The AlN film with a thick quasi-coherent layer and a less-tilted relaxed layer exhibited better crystallinity after FFA. This is the first comprehensive study to investigate the influence of sputtering and annealing conditions on the crystallinity of AlN films fabricated through RF sputtering using an AlN sintered target followed by FFA. The analysis method focusing on the thickness of the quasi-coherent layer and tilt disorder of the relaxed layer is useful to link the crystallinity of as-sputtered AlN with that of FFA Sp-AlN, and should be helpful in optimizing the fabrication process and improving the crystallinity of FFA Sp-AlN. In terms of future research, further investigation of other sputtering parameters, such as substrate temperature, RF power, and T–S distance, and detailed analysis on the characteristics of the AlN films with SIMS or TEM are necessary to improve the crystallinity of the FFA Sp-AlN and prove the schematic model of the recrystallization proposed in this work. Additionally, the optical characteristics, such as the diffractive indices and absorption coefficient of the AlN, and their dependences on the sputtering parameters should be considered for applying the FFA Sp-AlN to optical devices. The findings obtained herein should serve to improve the crystallinity of AlN templates fabricated through sputtering deposition followed by high-temperature annealing, which contribute to the performance improvement of DUV-LEDs.

Author Contributions: Funding acquisition, K.U., K.S., S.K. and H.M.; Investigation, K.U.; Supervision, H.M. Writing—Original draft, K.U. Writing—Review and editing, K.U., K.S., S.X., S.K. and H.M. All authors have read and agreed to the published version of the manuscript.

Funding: This work was partially supported by the Ministry of Education, Culture, Sports, Science, and Technology under the "Program for Building Regional Innovation Ecosystems", the JSPS KAKENHI grant under grant numbers JP16H06415, JP19K15025, JP21K04903, and JP21K14545, JST CREST under grant number 16815710, JST aXis under grant number JPMJAS2011, Ministry of Economy, Trade and Industry Monozukuri R&D Support Grant Program for SMEs Grant Number JPJ005698, and NEDO leading research program.

Institutional Review Board Statement: Not applicable.

Informed Consent Statement: Not applicable.

Data Availability Statement: The data that support the findings of this study are available within this article.

Conflicts of Interest: The authors declare no conflict of interest.

References

1. Kneissl, M.; Seong, T.-Y.; Han, J.; Amano, H. The emergence and prospects of deep-ultraviolet light-emitting diode technologies. *Nat. Photon.* **2019**, *13*, 233–244. [CrossRef]
2. Liu, S.; Luo, W.; Li, D.; Yuan, Y.; Tong, W.; Kang, J.; Wang, Y.; Li, D.; Rong, X.; Wang, T.; et al. Sec-eliminating the SARS-CoV-2 by AlGaN based high power deep ultraviolet light source. *Adv. Funct. Mater.* **2021**, *31*, 2008452. [CrossRef]
3. Ban, K.; Yamamoto, J.-I.; Takeda, K.; Ide, K.; Iwaya, M.; Takeuchi, T.; Kamiyama, S.; Akasaki, I.; Amano, H. Internal quantum efficiency of whole-composition-range AlGaN multiquantum wells. *Appl. Phys. Express* **2011**, *4*, 052101. [CrossRef]
4. Ruschel, J.; Glaab, J.; Susilo, N.; Hagedorn, S.; Walde, S.; Ziffer, E.; Cho, H.K.; Ploch, N.L.; Wernicke, T.; Weyers, M.; et al. Reliability of UVC LEDs fabricated on AlN/sapphire templates with different threading dislocation densities. *Appl. Phys. Lett.* **2020**, *117*, 241104. [CrossRef]
5. Kumagai, Y.; Kubota, Y.; Nagashima, T.; Kinoshita, T.; Dalmau, R.; Schlesser, R.; Moody, B.; Xie, J.; Murakami, H.; Koukitu, A.; et al. Preparation of a freestanding AlN substrate from a thick AlN layer grown by hydride vapor phase epitaxy on a bulk AlN substrate prepared by physical vapor transport. *Appl. Phys. Express* **2012**, *5*, 055504. [CrossRef]
6. Li, D.; Jiang, K.; Sun, X.; Guo, C. AlGaN photonics: Recent advances in materials and ultraviolet devices. *Adv. Opt. Photon.* **2018**, *10*, 43–110. [CrossRef]
7. Miyake, H.; Nishio, G.; Suzuki, S.; Hiramatsu, K.; Fukuyama, H.; Kaur, J.; Kuwano, N. Annealing of an AlN buffer layer in N_2–CO for growth of a high-quality AlN film on sapphire. *Appl. Phys. Express* **2016**, *9*, 025501. [CrossRef]
8. Miyake, H.; Lin, C.-H.; Tokoro, K.; Hiramatsu, K. Preparation of high-quality AlN on sapphire by high-temperature face-to-face annealing. *J. Cryst. Growth* **2016**, *456*, 155–159. [CrossRef]
9. Susilo, N.; Hagedorn, S.; Jaeger, D.; Miyake, H.; Zeimer, U.; Reich, C.; Neuschulz, B.; Sulmoni, L.; Guttmann, M.; Mehnke, F.; et al. AlGaN-based deep UV LEDs grown on sputtered and high temperature annealed AlN/sapphire. *Appl. Phys. Lett.* **2018**, *112*, 041110. [CrossRef]
10. Ni, R.; Chuo, C.-C.; Yang, K.; Ai, Y.; Zhang, L.; Cheng, Z.; Liu, Z.; Jia, L.; Zhang, Y. AlGaN-based ultraviolet light-emitting diode on high-temperature annealed sputtered AlN template. *J. Alloys Compd.* **2019**, *794*, 8–12. [CrossRef]
11. Huang, C.-Y.; Wu, P.-Y.; Chang, K.-S.; Lin, Y.-H.; Peng, W.-C.; Chang, Y.-Y.; Li, J.-P.; Yen, H.-W.; Wu, Y.S.; Miyake, H.; et al. High-quality and highly-transparent AlN template on annealed sputter-deposited AlN buffer layer for deep ultra-violet light-emitting diodes. *AIP Adv.* **2017**, *7*, 055110. [CrossRef]
12. Xiao, S.; Suzuki, R.; Miyake, H.; Harada, S.; Ujihara, T. Improvement mechanism of sputtered AlN films by high-temperature annealing. *J. Cryst. Growth* **2018**, *502*, 41–44. [CrossRef]
13. Zhao, L.; Yang, K.; Ai, Y.; Zhang, L.; Niu, X.; Lv, H.; Zhang, Y. Crystal quality improvement of sputtered AlN film on sapphire substrate by high-temperature annealing. *J. Mater. Sci. Mater. Electron.* **2018**, *29*, 13766–13773. [CrossRef]
14. Hagedorn, S.; Walde, S.; Mogilatenko, A.; Weyers, M.; Cancellara, L.; Albrecht, M.; Jaeger, D. Stabilization of sputtered AlN/sapphire templates during high temperature annealing. *J. Cryst. Growth* **2019**, *512*, 142–146. [CrossRef]
15. Uesugi, K.; Hayashi, Y.; Shojiki, K.; Miyake, H. Reduction of threading dislocation density and suppression of cracking in sputter-deposited AlN templates annealed at high temperatures. *Appl. Phys. Express* **2019**, *12*, 065501. [CrossRef]
16. Wang, D.; Uesugi, K.; Xiao, S.; Norimatsu, K.; Miyake, H. Low dislocation density AlN on sapphire prepared by double sputtering and annealing. *Appl. Phys. Express* **2020**, *13*, 095501. [CrossRef]
17. Wang, D.; Uesugi, K.; Xiao, S.; Norimatsu, K.; Miyake, H. High-quality AlN/sapphire templates prepared by thermal cycle annealing for high-performance ultraviolet light-emitting diodes. *Appl. Phys. Express* **2021**, *14*, 035505. [CrossRef]
18. Gu, W.; Liu, Z.; Guo, Y.; Wang, X.; Jia, X.; Liu, X.; Zeng, Y.; Wang, J.; Li, J.; Yan, J. Comprehensive study of crystalline AlN/sapphire templates after high-temperature annealing with various sputtering conditions. *J. Semicond.* **2020**, *41*, 122802. [CrossRef]
19. Mogami, Y.; Motegi, S.; Osawa, A.; Osaki, K.; Tanioka, Y.; Maeoka, A.; Jo, M.; Maeda, N.; Yaguchi, H.; Hirayama, H. Evolution of morphology and crystalline quality of DC-sputtered AlN films with high-temperature annealing. *Jpn. J. Appl. Phys.* **2019**, *58*, SC1029. [CrossRef]
20. Wang, M.X.; Xu, F.J.; Xie, N.; Sun, Y.H.; Liu, B.Y.; Ge, W.K.; Kang, X.N.; Qin, Z.X.; Yang, X.L.; Wang, X.Q.; et al. High-temperature annealing induced evolution of strain in AlN epitaxial films grown on sapphire substrates. *Appl. Phys. Lett.* **2019**, *114*, 112105. [CrossRef]
21. Walde, S.; Hagedorn, S.; Weyers, M. Impact of intermediate high temperature annealing on the properties of AlN/sapphire templates grown by metalorganic vapor phase epitaxy. *Jpn. J. Appl. Phys.* **2019**, *58*, SC1002. [CrossRef]
22. Itokazu, Y.; Kuwaba, S.; Jo, M.; Kamata, N.; Hirayama, H. Influence of the nucleation conditions on the quality of AlN layers with high-temperature annealing and regrowth processes. *Jpn. J. Appl. Phys.* **2019**, *58*, SC1056. [CrossRef]
23. Washiyama, S.; Guan, Y.; Mita, S.; Collazo, R.; Sitar, Z. Recovery kinetics in high temperature annealed AlN heteroepitaxial films. *J. Appl. Phys.* **2020**, *127*, 115301. [CrossRef]
24. Nemoz, M.; Dagher, R.; Matta, S.; Michon, A.; Vennéguès, P.; Brault, J. Dislocation densities reduction in MBE-grown AlN thin films by high-temperature annealing. *J. Cryst. Growth* **2017**, *461*, 10–15. [CrossRef]
25. Yoshizawa, R.; Miyake, H.; Hiramatsu, K. Effect of thermal annealing on AlN films grown on sputtered AlN templates by metalorganic vapor phase epitaxy. *Jpn. J. Appl. Phys.* **2018**, *57*, 01AD05. [CrossRef]
26. Ben, J.; Sun, X.; Jia, Y.; Jiang, K.; Shi, Z.; Liu, H.; Wang, Y.; Kai, C.; Wu, Y.; Li, D. Defect evolution in AlN templates on PVD-AlN/sapphire substrates by thermal annealing. *CrystEngComm* **2018**, *20*, 4623–4629. [CrossRef]

27. Kuboya, S.; Uesugi, K.; Shojiki, K.; Tezen, Y.; Norimatsu, K.; Miyake, H. Crystalline quality improvement of face-to-face annealed MOVPE-grown AlN on vicinal sapphire substrate with sputtered nucleation layer. *J. Cryst. Growth* **2020**, *545*, 125722. [CrossRef]
28. Darakchieva, V.; Birch, J.; Schubert, M.; Paskova, T.; Tungasmita, S.; Wagner, G.; Kasic, A.; Monemar, B. Strain-related structural and vibrational properties of thin epitaxial AlN layers. *Phys. Rev. B* **2004**, *70*, 045411. [CrossRef]
29. Tanaka, S.; Shojiki, K.; Uesugi, K.; Hayashi, Y.; Miyake, H. Quantitative evaluation of strain relaxation in annealed sputter-deposited AlN film. *J. Cryst. Growth* **2019**, *512*, 16–19. [CrossRef]
30. Miceli, P.F.; Palmstrom, C.J. X-ray scattering from rotational disorder in epitaxial films: An unconventional mosaic crystal. *Phys. Rev. B* **1995**, *51*, 5506–5509. [CrossRef] [PubMed]
31. Metzger, T.; Höpler, R.; Born, E.; Christiansen, S.; Albrecht, M.; Strunk, H.P.; Ambacher, O.; Stutzmann, M.; Stömmer, R.; Schuster, M.; et al. Coherent X-ray scattering phenomenon in highly disordered epitaxial AlN films. *Phys. Status Solidi (a)* **1997**, *162*, 529–535. [CrossRef]
32. Kang, H.C.; Seo, S.H.; Noh, D.Y. X-ray scattering study on the structural evolution of AlN/sapphire(0001) films during radiofrequency sputter growth. *J. Mater. Res.* **2001**, *16*, 1814–1821. [CrossRef]
33. Williamson, G.; Hall, W. X-ray line broadening from filed aluminium and wolfram. *Acta Met.* **1953**, *1*, 22–31. [CrossRef]
34. Metzger, T.; Höpler, R.; Born, E.; Ambacher, O.; Stutzmann, M.; Stömmer, R.; Schuster, M.; Göbel, H.; Christiansen, S.; Albrecht, M.; et al. Defect structure of epitaxial GaN films determined by transmission electron microscopy and triple-axis X-ray diffractometry. *Philos. Mag. A* **1998**, *77*, 1013–1025. [CrossRef]
35. Chierchia, R.; Böttcher, T.; Heinke, H.; Einfeldt, S.; Figge, S.; Hommel, D. Microstructure of heteroepitaxial GaN revealed by x-ray diffraction. *J. Appl. Phys.* **2003**, *93*, 8918–8925. [CrossRef]
36. Uesugi, K.; Shojiki, K.; Tezen, Y.; Hayashi, Y.; Miyake, H. Suppression of dislocation-induced spiral hillocks in MOVPE-grown AlGaN on face-to-face annealed sputter-deposited AlN template. *Appl. Phys. Lett.* **2020**, *116*, 062101. [CrossRef]
37. Shojiki, K.; Ishii, R.; Uesugi, K.; Funato, M.; Kawakami, Y.; Miyake, H. Impact of face-to-face annealed sputtered AlN on the optical properties of AlGaN multiple quantum wells. *AIP Adv.* **2019**, *9*, 125342. [CrossRef]
38. Shojiki, K.; Uesugi, K.; Kuboya, S.; Inamori, T.; Kawabata, S.; Miyake, H. High-quality AlN template prepared by face-to-face annealing of sputtered AlN on sapphire. *Phys. Status Solidi (b)* **2021**, *258*, 2000352. [CrossRef]